Supporting Information

Supercurrent Flow in Multiterminal Graphene Josephson Junctions

Anne W. Draelos,[†] Ming-Tso Wei,[†] Andrew Seredinski,[†] Hengming Li,[‡] Yash Mehta,[‡] Kenji Watanabe,[¶] Takashi Taniguchi,[¶] Ivan V. Borzenets,[*,§] François Amet,[‡] and Gleb Finkelstein[*,†]

†*Department of Physics, Duke University, Durham, North Carolina 27708, United States*

‡*Department of Physics and Astronomy, Appalachian State University, Boone, North Carolina 28607, United States*

¶*Advanced Materials Laboratory, NIMS, Tsukuba 305-0044, Japan*

§*Department of Physics, City University of Hong Kong, Kowloon, Hong Kong SAR*

E-mail: iborzene@cityu.edu.hk; gleb@phy.duke.edu

1. Initial sample characterization

Figure S1(a) shows an optical image of the multiterminal device alongside reference junctions made from the same graphene-hBN stack. Each side of the square device is singly contacted with the superconductor MoRe, before diverging into two or three separate leads for bonding. This is also the case for the reference junctions.

Due to complex electron flow in the multiterminal junction, characterization of the graphene crystal quality is difficult. Instead, here we present transport measurements conducted on a two-terminal reference junction of width 3μm and length 500 nm taken at 3K. Figure S1(b) presents the normal state differential resistance R_N of this junction as a function of back gate voltage. MoRe contacts locally n-dope the graphene, which results in the formation of n-p-n junctions in the case of bulk p-doping. For a ballistic sample, this leads to Fabry-Pérot oscillations in resistance for negative back gate voltages, which are present in this device.[1] Such oscillations are also visible in the critical current of the junction,[2] shown in Figure S1(c), which plots the voltage across the sample as a function of bias current I_{Bias} and back gate voltage V_G.

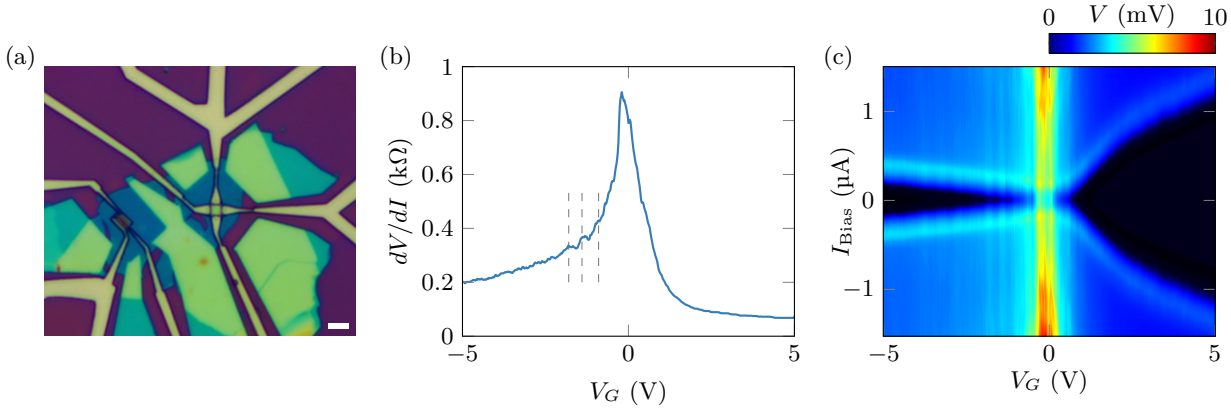

Figure S1: (a) Optical image of the sample (scale bar 3 μm). The main multiterminal sample is centered in the image. To the left of the main sample are two standard two-terminal junctions made on the same graphene-hBN stack as the main sample. (b) Gate dependence of the reference junction normal resistance R_N. The gray dashed lines mark the positions of a few Fabry-Pérot resonances with respect to V_G. (c) Map of voltage vs bias current I_{Bias} and back gate voltage V_G for a reference junction. The Fabry-Pérot resonances appear at the same gate positions as in the R_N map.

2. Signature of ballistic transport

Here we demonstrate the ballistic nature of supercurrent in our system. We approach this by looking at the behavior of the critical current I_C with respect to the Josephson junction length and temperature. For electron transport in the ballistic regime we have: $I_C R_N \propto \delta E$, where $\delta E = \hbar v_F / 2\pi L$.[3–5] Here, R_N is the normal resistance, v_F is the Fermi velocity, and L is the length of the junction. In the diffusive regime the critical current is: $I_C R_N \propto E_{Th}$.[6,7] E_{Th} is the Thouless energy and is equal to $E_{Th} = \hbar D / L^2$, where D is the coefficient of diffusion. Therefore, for the ballistic case $I_C R_N \propto 1/L$, while in the diffusive case $I_C R_N \propto 1/L^2$. We compare the critical currents (at the same heating power) between the left-bottom (LB) and top-bottom (TB) junctions. The LB junction has: $I_C = 88nA$, $R_N = 330\Omega$, $L = 500nm$. The TB junction has: $I_C = 24nA$, $R_N = 330\Omega$, $L = 2000nm$. One can see that the value $I_C R_N L$ remains constant between the two junctions; that is, $I_C R_N$ scales linearly with L, which is indicative of ballistic supercurrent. (If the junction were in the diffusive regime, the supercurrent in the TB junction would be much more suppressed than in the LB junction.)

We now look at the temperature dependence of the critical current I_C in the LB junction. For a Josephson junction in the long ballistic regime, the critical current scales with temperature as $\log I_C \propto -\frac{k_B T}{\delta E}$.[3–5] For the case of the diffusive regime the critical current scales as $\log I_C \propto -\sqrt{\frac{2\pi k_B T}{E_{TH}}}$.[6] Figure S2 shows the measurement of I_C vs T plotted together with the fitted curve for both the ballistic (red) and diffusive (blue) regimes. The ballistic regime results in a better fit and returns $\delta E = 143\mu eV$, which translates to a junction length of 580 nm (similar to the designed distance between the contacts). The fit to a diffusive regime returns a Thouless energy $E_{Th} = 377\mu eV$ (a rather large value), which given the junction width $W \approx 700$ nm and the gate voltage $V_G = 5V$ returns a junction length of ≈ 2000 nm: an unrealistic value for the LB junction. As the critical current behavior of the device matches the long ballistic regime well, and does not match the diffusive regime, we conclude that the device operates in the long ballistic junction regime.

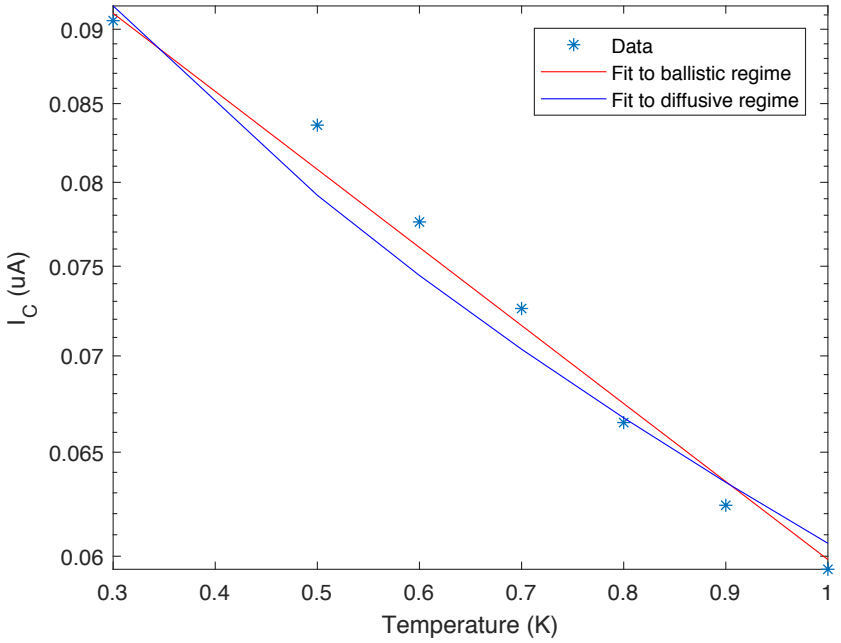

Figure S2: Critical current I_C of the LB junction plotted versus temperature T on a semilog scale. The data points are fit to either the long ballistic (red) or the diffusive (blue) regime. The expression for the long ballistic junction better describes the data, as stated in the accompanying text.

3. Gate dependence

The measurements presented in the main text were all taken at a back gate voltage V_G = 5 V, in the n-doping regime. Figure S3 presents maps of differential resistances of the left-bottom (LB) and right-bottom (RB) junctions at different gate voltages: 4 V, 2 V, 0 V, -1 V, and -3 V (where the Dirac point is at $V_G \sim 0.5$ V). All superconducting features are controllably tuned with the back gate. As expected, the critical current decreases at lower doping in both the central region and in the extended "arms". At $V_G = 0$ V, for example, a small central dot is the only surviving superconducting feature (Fig. S3e,f). The angles of the supercurrent arms also vary slightly with back gate, as the resistance of each junction changes and consequently modifies the equal potential conditions between pairs of terminals.

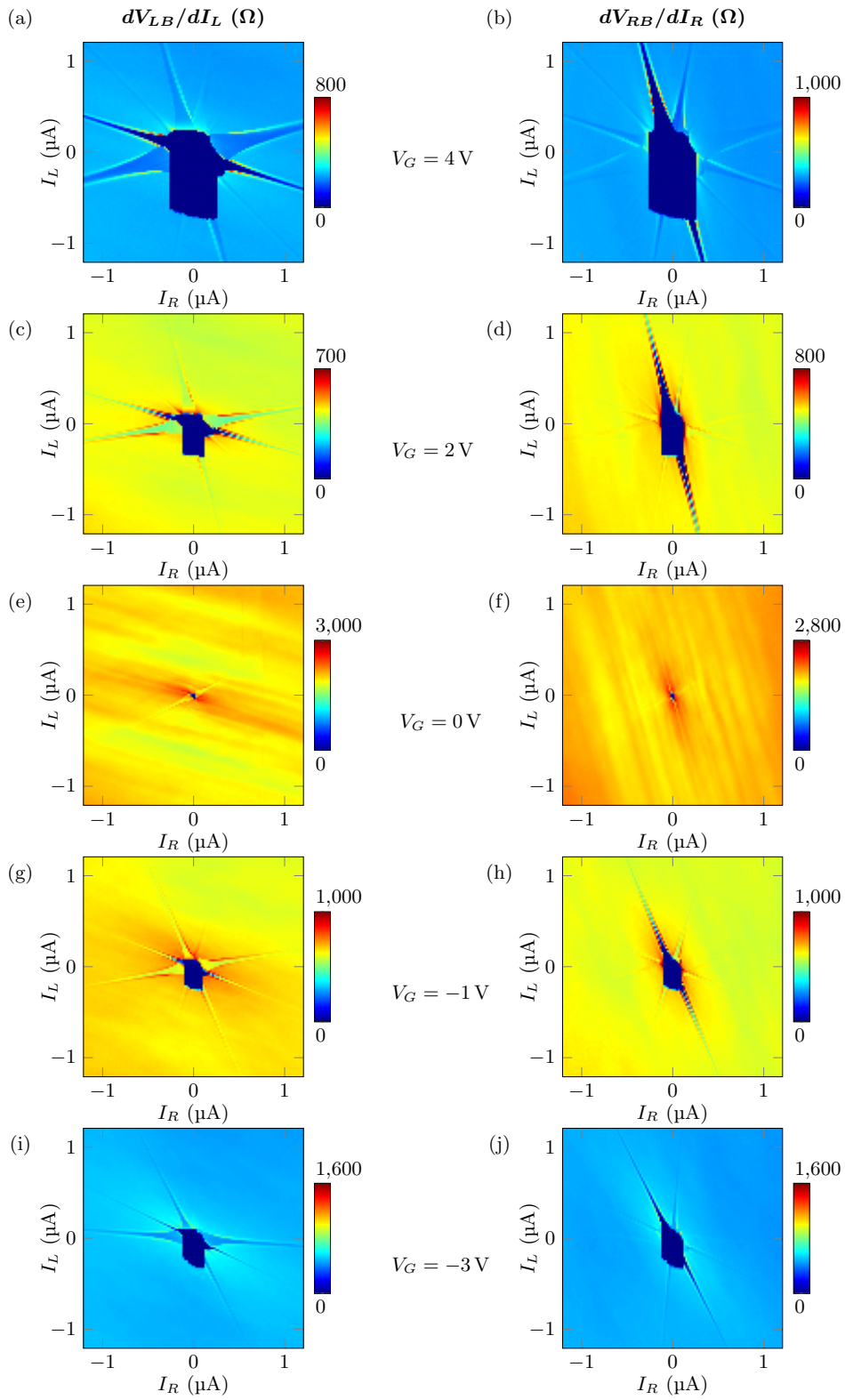

Figure S3: Differential resistances dV_{LB}/dI_L (left column) and dV_{RB}/dI_R (right column) measured at different gate voltages: (a,b) 4 V, (c,d) 2 V, (e,f) 0 V, (g,h) -1 V, and (i,j) -3 V.

4. Direct voltage measurement between top and bottom contacts

The middle panel of Figure S4 shows the absolute voltage difference measured directly between the top and bottom (grounded) contacts, at $V_G = -3V$. Bias current was supplied to the right and left contacts as before. The central dark region of zero voltage extends along a diagonal, following the annotated dashed line. The concurrently measured differential resistance maps of the left-bottom and right-bottom junctions show the identified top-bottom supercurrent feature as a faint diagonal line (Fig. S4(a,c)).

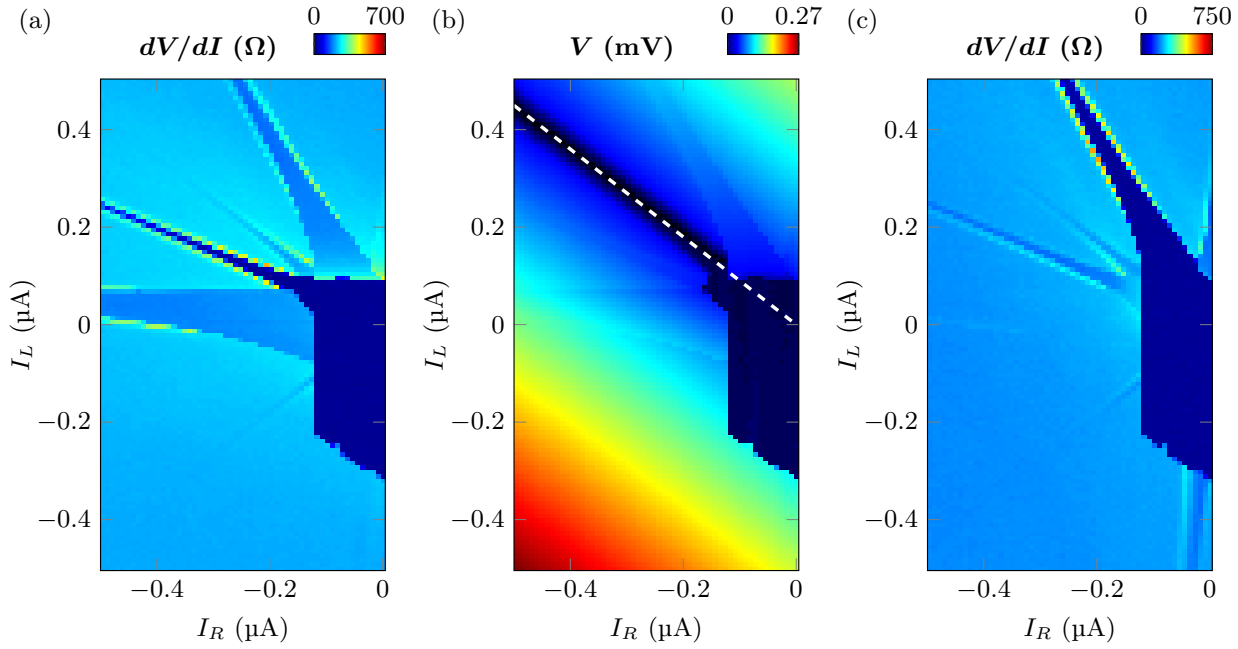

Figure S4: (a,c) Maps of the differential resistance of the bottom-left and bottom-right junctions, respectively. (b) dc voltage map $|V_{TB}|$ between the top and bottom contacts.

5. Rotated measurement scheme

Here we present additional measurements with the sample rotated by 90 degrees compared to the setup used in the main text. First, we move the ground terminal to the left contact, and all other components are moved in kind relative to that ground (Fig. S5a). The differential resistances and dc voltages of the left-bottom (LB) and top-left (TL) junctions are shown in Fig. S5(b-e), and are qualitatively similar to the original measurements in the main text. Next, we flip the ground across to the right contact, but leave the voltage probes and current sources in place (Fig. S5f). The resulting maps appear qualitatively similar, but at this point we are measuring the resistances between the current-sourcing leads T, B and the left contact which is now floating. The deepest features in the maps then correspond to supercurrents in junctions not adjacent to the grounded contact. This observation further confirms our identification of minor features in Figure 1 of the main paper.

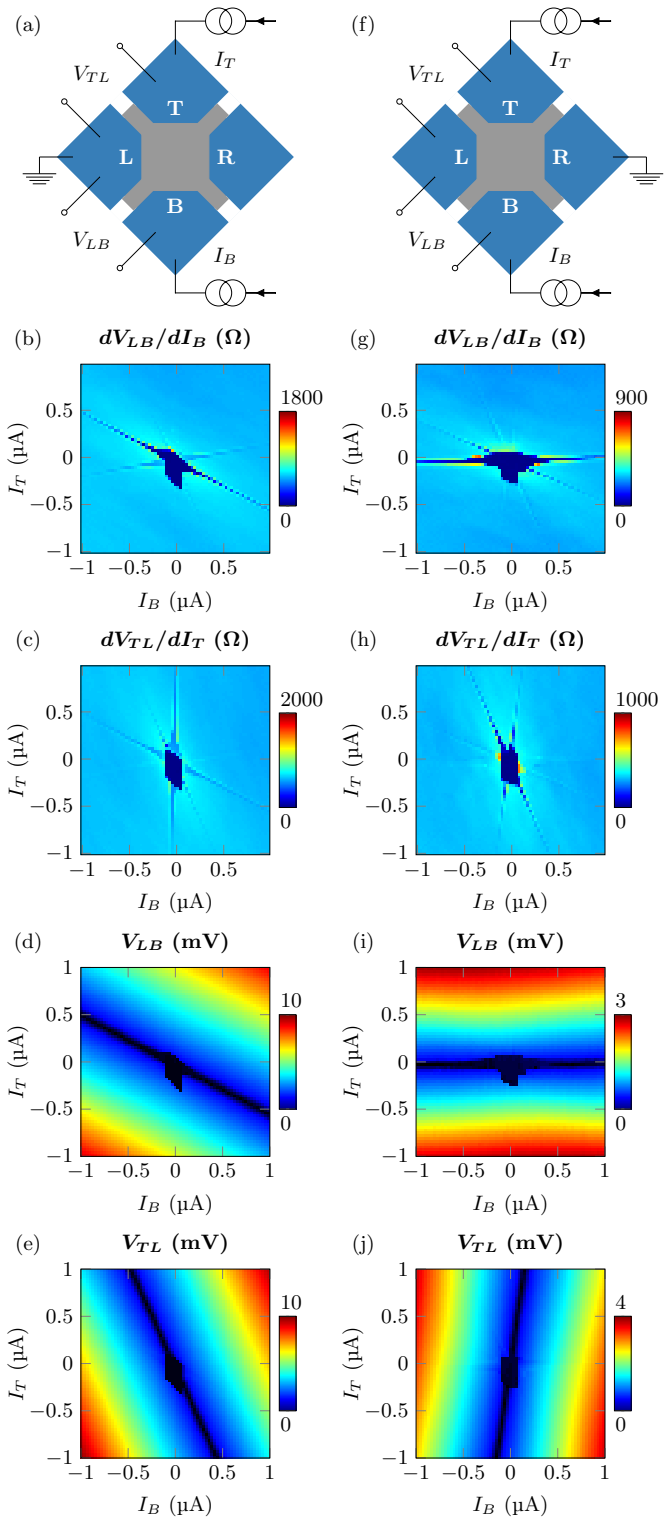

Figure S5: (a,f) Diagrams of the sample in the rotated configurations. Column (b-e): Differential resistances and dc voltages of the junctions adjacent to the grounded contact in configuration (a). Column (g-j): Similar maps for the junctions nonadjacent to the grounded contact in configuration (f).

6. Interchanged bias sweep order

The measurements presented in the main text were all made with the right bias current stepped slowly, and the left bias current swept quickly, so all the maps were raster scanned in the vertical direction. Thus the differences between switching and retrapping currents are most easily observed in the vertical direction in our maps. Here we also present a map measured by stepping the left bias current slowly, and sweeping the right bias current quickly, plotted using the same axes (Fig. S6). The central region is changed, and the differences between switching and retrapping are now obvious in the horizontal direction. However, the diagonal arms of supercurrent extending from this central region are unchanged.

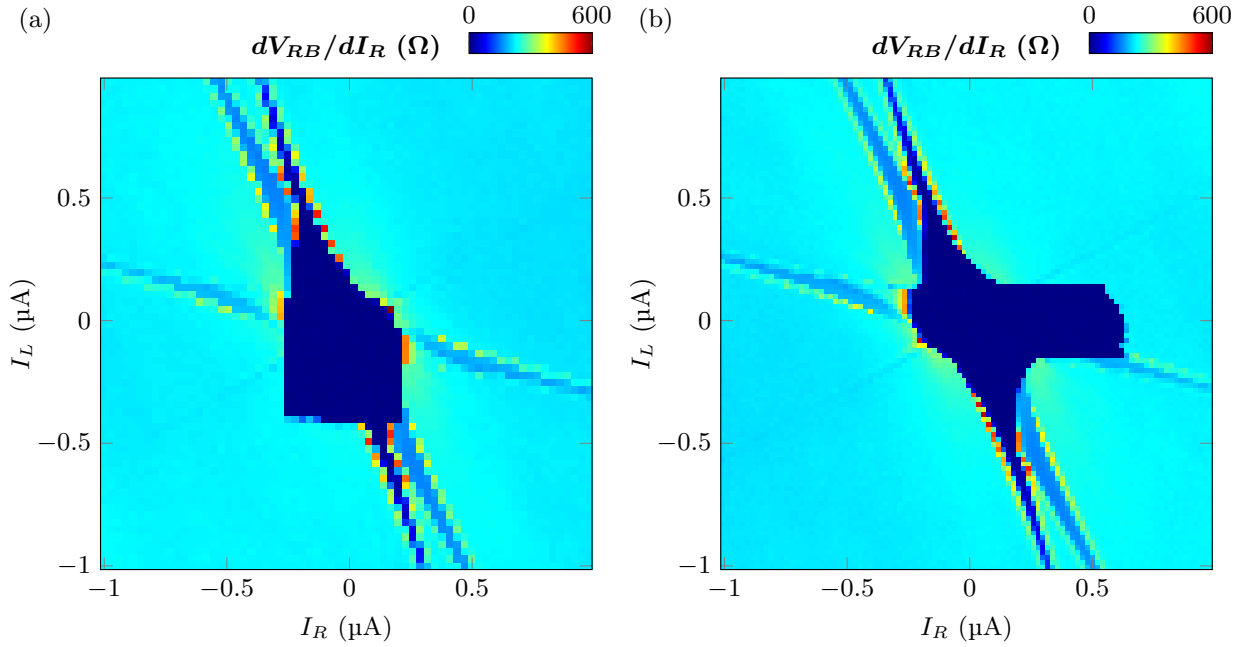

Figure S6: (a) Differential resistance dV_{RB}/dI_R measured using the original bias sweep order, at V_G = -1.75 V. (b) The same junction measured by first stepping the left current bias and then sweeping the right current from negative to positive. Only the shape of the dark central superconducting region is changed.

7. SPICE simulations

Here we present the results of three different simulations where: all R are equal; left and right junctions are imbalanced; or top and bottom junctions are imbalanced. Figure S7(a,b) are the maps from the left-bottom and right-bottom junctions, respectively, in the scenario where all sides of the square are equal and the diagonal junctions (top-bottom and left-right) are twice as resistive. Note here that the angular distribution of the various arms of supercurrent is more uniform. To model a left-right imbalance, we simulated a network where the left-bottom and left-top junctions are half as resistive as the right-bottom and right-top junctions (Fig. S7(c,d)). Finally, to model a top-bottom imbalance we set the left-top and right-top junctions to be half as resistive as the left-bottom and right-bottom junctions (Fig. S7(e,f)). All resistor values for each simulated network, including the network modeled in the main text, are recorded in Table S1.

Table S1: The six resistor values for each simulated network.

Network	R_{LB} (Ω)	R_{RB} (Ω)	R_{TL} (Ω)	R_{TR} (Ω)	R_{LR} (Ω)	R_{TB} (Ω)
Main text	330	430	280	440	1370	330
Equal R	500	500	500	500	1000	1000
LR imbalance	300	600	300	600	1000	1000
TB imbalance	600	600	300	300	1000	1000

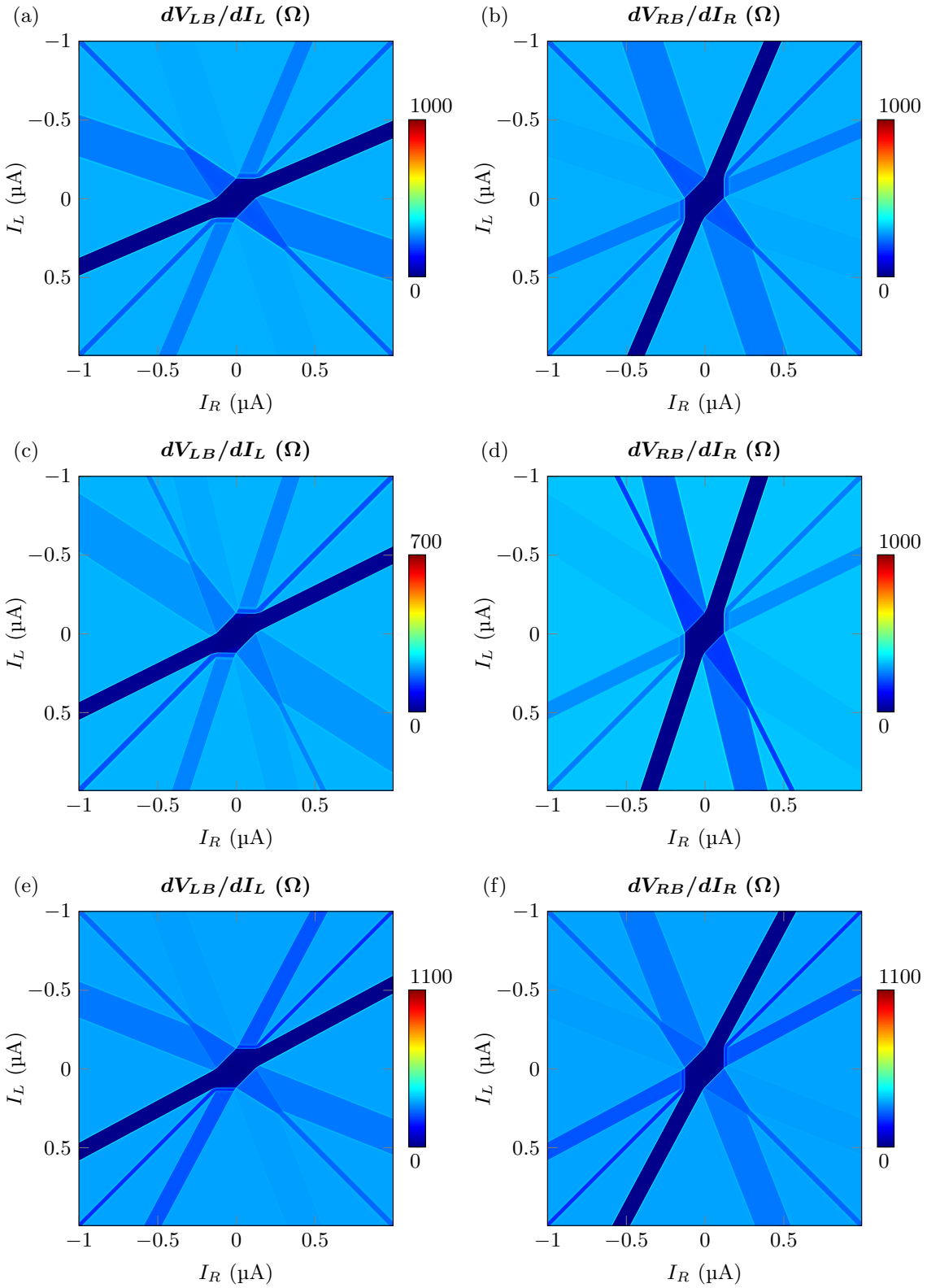

Figure S7: (a,b) Simulated maps for equal R, (c,d) left-right imbalance, and (e,f) top-bottom imbalance.

References

(1) Young, A. F.; Kim, P. Quantum interference and Klein tunnelling in graphene heterojunctions. *Nature Physics* **2009**, 5, 222. DOI: 10.1038/NPHYS1198

(2) Ben Shalom, M.; Zhu, M. J.; Fal'ko, V. I.; Mishchenko, A.; Kretinin, A. V.; Novoselov, K. S.; Woods, C. R.; Watanabe, K.; Taniguchi, T.; Geim, A. K.; Prance, J. R. Quantum oscillations of the critical current and high-field superconducting proximity in ballistic graphene. *Nature Physics* **2016**, 12, 318. DOI: 10.1038/nphys3592

(3) Kulik, I. O. Macroscopic Quantization and the Proximity Effect in S-N-S Junctions. *Sov. Phys. JETP* **1970**, 30, 5, pp. 944.

(4) Bardeen, J.; Johnson, J. L. Josephson Current Flow in Pure Superconducting-Normal-Superconducting Junctions. *Phys. Rev. B* **1972**, 5, 72. DOI: 10.1103/PhysRevB.5.72

(5) Borzenets, I. V.; Amet, F.; Ke, C. T.; Draelos, A. W.; Wei, M. T.; Seredinski, A.; Watanabe, K.; Taniguchi, T.; Bomze, Y.; Yamamoto, M.; Tarucha, S.; Finkelstein, G. Ballistic Graphene Josephson Junctions from the Short to the Long Junction Regimes. *Phys. Rev. Lett.* **2016**, 117, 237002. DOI: 10.1103/PhysRevLett.117.237002

(6) Dubos, P.; Courtois, H.; Pannetier, B.; Wilhelm, F.; Zaikin, A.D.; Schon, G. Josephson critical current in a long mesoscopic S-N-S junction. *Phys. Rev. B* **2001**, 63, 064502. DOI: 10.1103/PhysRevB.63.064502

(7) Ke, C. T.; Borzenets, I. V.; Draelos, A. W.; Amet, F.; Bomze, Y.; Jones, G.; Craciun, M.; Russo, S.; Yamamoto, M.; Tarucha, S; Finkelstein, G. Critical Current Scaling in Long Diffusive Graphene-Based Josephson Junctions. *Nanoletters* **2016**, 16, 8, pp. 4788. DOI: 10.1021/acs.nanolett.6b00738